Supplementary Information

Binary superlattices enable programmable tensile strength and ductility in magneto-elastic granular architectures (MEGAs)

1 Supplementary figures

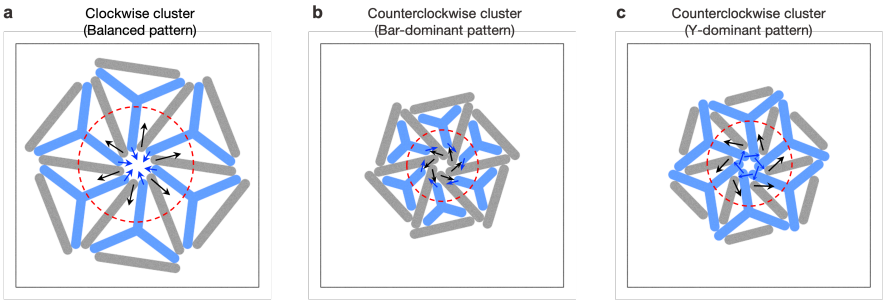

System		a	b	c
Node binding motif		12-magnet ring 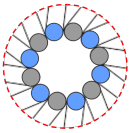	6-magnet ring 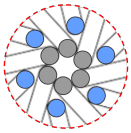	6-magnet ring 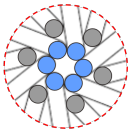
Magnetic interaction energy (all pairs) [J]	Bar–Bar	0.0035	**-0.0244**	-0.0015
	Y–Y	0.0032	-0.0011	**-0.0246**
	Bar–Y	**-0.0331**	-0.0023	-0.0029
	Total	-0.0263	-0.0278	-0.0290
Nearest-neighbor magnetic interaction energy (per pair) [J]		Bar–Y: -0.00249	Bar–Bar: -0.00347	Y–Y: -0.00352
Unit cell area [m²]		0.0053	0.0022	0.0027

Supplementary Fig. 1 Magnetic cluster configurations and energies. a–c, Magnetic clusters in the balanced (a), Bar-dominant (b), and Y-dominant (c) patterns. Nodes are formed by a twelve-magnet ring with alternating Bar and Y ends (a), or by a six-magnet ring composed only of Bar ends (b) or Y ends (c). Black and blue arrows indicate dipole orientations of Bar and Y ends within the red dashed circled region. Panels correspond to the insets in Fig. 2a–c of the main text. The table summarizes node structures and corresponding magnetic interaction energies, with dominant contributions highlighted.

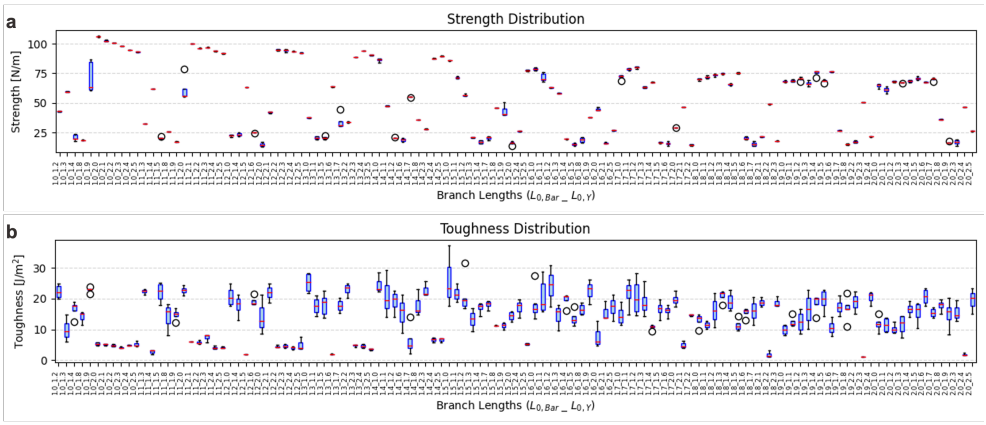

Supplementary Fig. 2 Tensile response of all contracted Bar–Y superlattices examined in the simulation. a,b, Distributions of strength (a) and toughness (b), each including at least three data points from independent replicates.

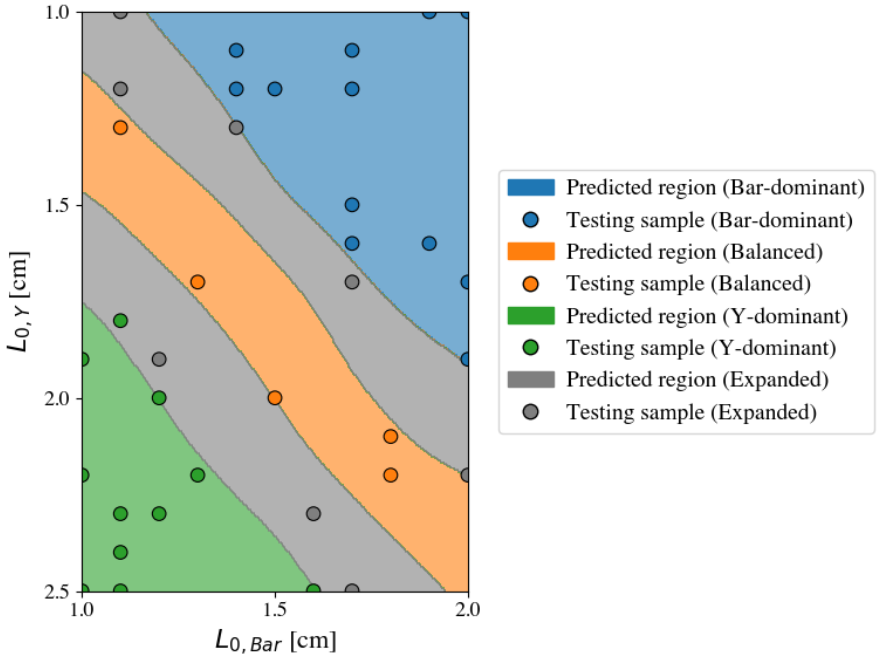

Supplementary Fig. 3 Predicted decision regions of different configuration types using the trained GPC. The colored background indicates the classification regions, while the circles represent the testing samples. The classifier achieves an accuracy of 94.4% on the test set.

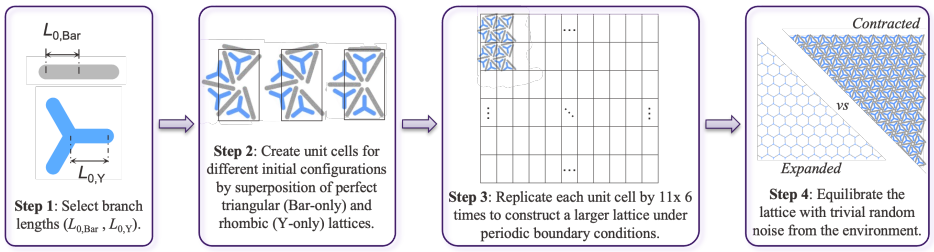

Supplementary Fig. 4 Schematic illustrating the generation and equilibration process of binary Bar–Y superlattices in the simulation.

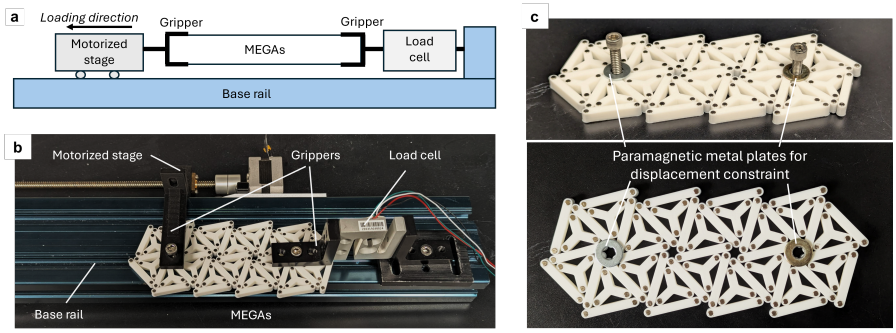

Supplementary Fig. 5 Experimental tensile test setup and boundary constraints. a,b, Schematic (a) and experimental setup (b) of the customized uniaxial tensile test platform for MEGAs. c, Details of the boundary constraints implemented during the tensile test, where the displacements of the boundary units are restricted by paramagnetic metal plates.

2 Expanded Bar–Y systems

The free equilibration simulation of a binary Bar–Y system with $(L_{0,\mathrm{Bar}}, L_{0,\mathrm{Y}}) = (1.3, 1.3)$ is shown in Supplementary Fig. 6. This system lies within one of the expanded bands of the phase map shown in Fig. 1d of the main text. Supplementary Fig. 6a presents the evolution of the magnetic interaction energy of the system during equilibration, and Supplementary Fig. 6b shows the corresponding deformation states. The initial configuration (i) was constructed following the same procedure described in Methods of the main text. Once free equilibration begins, strong repulsive forces between neighboring magnetic units cause them to pivot about their joints and rotate outward, leading to a rapid drop in magnetic energy. At (iii), the system transitions to an ordered hexagon-like network. Eventually, the system settles into a stable hexagonal configuration with minimal magnetic energy, as shown at (iv).

To experimentally validate that the binary Bar–Y system cannot form a stable contracted configuration with the hybrid architecture, we manually compressed six Bar units and six Y units into a compact assembly (Supplementary Fig. 7 $t = 0$ s) and

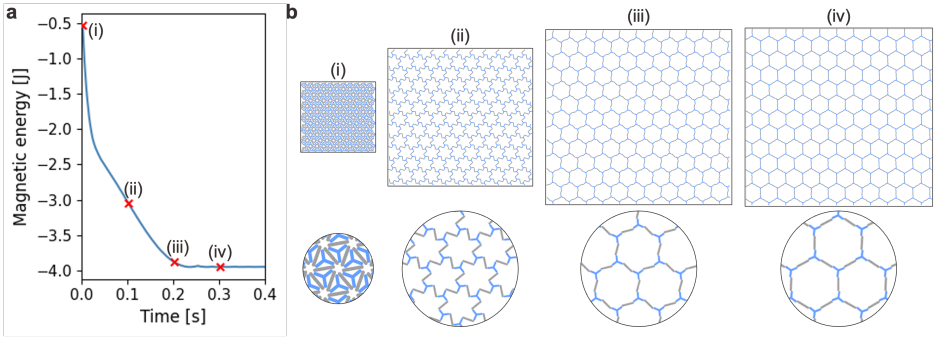

Supplementary Fig. 6 Free equilibration simulation of the binary system with $(L_{0,\mathrm{Bar}}, L_{0,\mathrm{Y}}) = (1.3, 1.3)$. a, Magnetic interaction energy evolution during the simulation. b, Representative deformed configurations from the initial state (i) to the final state (iv) as indicated in panel a, with an enlarged view shown below each configuration for better visualization.

then released all constraints simultaneously. Upon release, the system opens rapidly due to strong repulsion. The uniform constraints present in the reciprocal lattice in the simulation cannot be perfectly reproduced experimentally, resulting in non-uniform expansion. Nevertheless, the early deformation stage in the experiment ($t = 0.0169$ s and $t = 0.0339$ s in Supplementary Fig. 7) closely resembles state (ii) of the simulation, as shown in Supplementary Fig. 6b. The small assembly then expands to a fully stretched configuration with an irregular hexagonal pattern at $t = 0.3898$ s. It subsequently undergoes a brief oscillation, marked by alternating contraction and extension along two perpendicular directions, until the structure relaxes to a stable state at $t = 0.5593$ s, forming a regular hexagon very similar to state (iv) in Supplementary Fig. 6b. The expansion time from the initial compressed state to the fully stretched state (0.3898 s) is comparable to the simulation time (≈ 0.3 s). Notably, in the simulation, the movement of each hexagonal module is strongly constrained by neighboring units in the periodic lattice, so the apparent oscillatory behavior observed for an isolated hexagon in the experiment does not appear. Although the total time from the onset of motion to the final stable state is nearly twice that observed in the simulation, the timescales remain comparable. The deviation is within reasonable tolerance, given the non-uniform implementation and release of constraints, fabrication imperfections, and assembly errors in the proof-of-concept experiment.

A quasi-static uniaxial tensile test was also performed on this lattice in the simulation. The resulting stress–strain curve and deformation snapshots are shown in Supplementary Fig. 8a,b, respectively. Owing to the low magnetic interaction energy density within the hexagonal network, this expanded configuration exhibits much lower strength compared with contracted systems in Fig. 2 of the main text. The two-node binding between the Bar end and Y end provides significant rotational flexibility during pulling. The lattice finally fails with its hexagonal voids highly distorted (iii–iv). The full deformation trajectory is shown in Supplementary Video 1. Although the maximum strain prior to failure (0.399) is not as high as in some contracted systems, the overall deformation remains large given the large initial lattice size. This

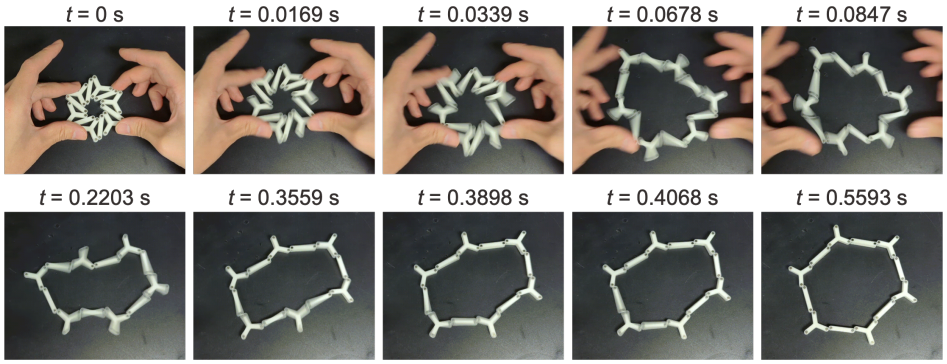

Supplementary Fig. 7 Free relaxation experiment on a small MEGA assembly of the binary system with $(L_{0,\mathrm{Bar}}, L_{0,\mathrm{Y}}) = (1.3, 1.3)$. Snapshots are from a 60-fps recording.

strain corresponds to a displacement of approximately 460 mm in the pulling direction. This two-node binding motif is robust across expanded systems with different branch lengths. Overall, hexagonal MEGA lattices possess substantial deformation capacity but remain very weak. Consequently, the discussion of binary Bar–Y MEGAs in this work focuses on contracted configurations, which are mechanically stronger and exhibit more diverse responses.

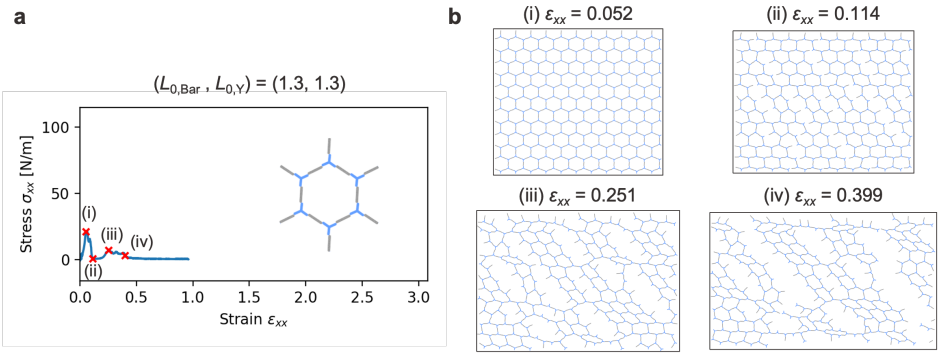

Supplementary Fig. 8 Uniaxial tensile simulation of the binary system with $(L_{0,\mathrm{Bar}}, L_{0,\mathrm{Y}}) = (1.3, 1.3)$. a, Stress–strain curve under loading. The insets show its magnetic cluster configuration, consisting of six Y units and twelve Bar units. b, Representative deformed configurations at the strains marked by red crosses in panel a.

3 Configurations of uniformly scaled Bar–Y systems

The main text examines equilibrated configurations of binary Bar–Y systems with branch lengths ranging from 1.0 to 2.5 cm and a fixed effective radius r_0. Here, we demonstrate that the observed equilibrated patterns are robust across different length scales when geometric parameters and magnetic strengths are adjusted appropriately.

Specifically, to preserve the equilibrated lattice pattern between systems of different sizes, all geometric parameters (including the Bar branch length $L_{0,\mathrm{Bar}}$, the Y branch length $L_{0,\mathrm{Y}}$, and the effective radius r_0) must be scaled by the same factor, C_{len}. This scaling preserves the same normalized unit-size difference ρ between the two systems, as defined in the main text. In addition, to ensure that the scaled system relaxes toward the energetically favorable configuration with the same lattice pattern, the magnitude of the magnetic dipole moment (i.e., the magnetic strength) of the embedded magnets must also be scaled accordingly.

The magnetostatic interaction energy $e_{\mathrm{mag},ij}$ between magnetic dipoles i and j is given by Equation (S1), where $\mathbf{m}_i$ and $\mathbf{m}_j$ denote the magnetic dipole moments of dipoles i and j, respectively, $\mathbf{r}_{ij}$ is the vector from dipole i to dipole j, and μ_0 is the vacuum permeability ($\mu_0 = 4\pi \times 10^{-7}\ \mathrm{H\,m^{-1}}$).

$$e_{\mathrm{mag},ij} = \frac{\mu_0}{4\pi}\left[\frac{\mathbf{m}_i \cdot \mathbf{m}_j}{r_{ij}^3} - \frac{3(\mathbf{m}_i \cdot \mathbf{r}_{ij})(\mathbf{m}_j \cdot \mathbf{r}_{ij})}{r_{ij}^5}\right] \tag{S1}$$

The magnetic interaction energy density of a MEGA lattice is defined as the total magnetostatic interaction energy within a unit cell divided by the unit cell area. For a scaled system in which all geometric parameters are scaled by C_{len}, and the magnitude of the magnetic dipole moment is scaled by C_{mag}, the magnetic interaction energy density scales approximately as $C_{\mathrm{mag}}^2 C_{\mathrm{len}}^{-5}$. This follows from the fact that the magnetic interaction energy scales as $C_{\mathrm{mag}}^2 C_{\mathrm{len}}^{-3}$ according to Equation (S1), while the unit cell area scales as C_{len}^2. Therefore, choosing $C_{\mathrm{mag}} = C_{\mathrm{len}}^{2.5}$ ensures that the scaled system has the same magnetic interaction energy density as the corresponding unscaled system, thereby largely preserving the relative energy landscape.

Based on this scaling rule, we randomly select a representative system from each region in Fig. 1e,f of the main text and generate initial configurations with the scaled Bar units, Y units, and magnetic strengths. The geometric scaling factor, C_{len}, is randomly selected for each system, while the magnetic strength scaling factor, C_{mag}, is set to $C_{\mathrm{len}}^{2.5}$. Free equilibration simulations are then performed using the same procedures described in the main text. Supplementary Table 1 summarizes the geometric parameters, magnet strengths, unit schematics, and equilibrated configurations for the scaled systems, together with the corresponding information for the original unscaled systems for direct comparison. As shown, under this scaling scheme, all systems recover the same equilibrated lattice patterns as their unscaled counterparts, demonstrating that our findings are not limited to the branch-length range explored in the main text.

4 Transitional mechanical behavior in balanced systems

The system with $(L_{0,\mathrm{Bar}}, L_{0,\mathrm{Y}}) = (1.4, 1.8)$ lies within the balanced-network regime (region II, orange) of the phase map and forms a clockwise-oriented magnetic cluster with a twelve-magnet binding motif. The equilibrated magnetic cluster of this system, shown in Supplementary Fig. 9a, is very similar to that of the system discussed in

Supplementary Table 1 Geometric parameters, normalized unit-size differences, magnet strengths, unit schematics, and equilibrated configurations for the scaled systems and their corresponding unscaled counterparts. Systems I-1(s), II-3(s), III-1(s), and E-2(s) correspond to scaled versions of I-1, II-3, III-1, and E-2, respectively, shown in Fig. 1e,f of the main text.

System	C_{len}	$L_{0,\text{Bar}}$ [cm]	$L_{0,\text{Y}}$ [cm]	r_0 [cm]	ρ	C_{mag}	m [A·m^2]	Unit schematics	Equilibrated configuration
I-1	1.0	2.00	1.00	0.239	9.5	1.00	0.0524	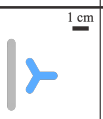	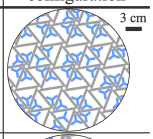
I-1(s)	1.5	3.00	1.50	0.358	9.5	2.76	0.1444		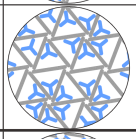
II-3	1.0	1.70	2.10	0.239	-1.0	1.00	0.0524		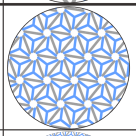
II-3(s)	0.4	0.68	0.84	0.096	-1.0	0.10	0.0053		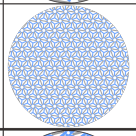
III-1	1.0	1.00	1.90	0.239	-5.4	1.00	0.0524		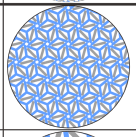
III-1(s)	2.0	2.00	3.80	0.478	-5.4	5.66	0.2965	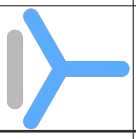	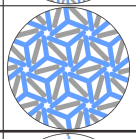
E-2	1.0	1.60	2.30	0.239	-3.3	1.00	0.0524		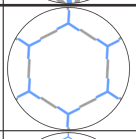
E-2(s)	0.5	0.80	1.15	0.119	-3.3	0.18	0.0093		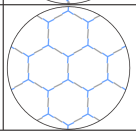

Fig. 2a with $(L_{0,\text{Bar}}, L_{0,\text{Y}}) = (1.9, 2.3)$ in the main text. The corresponding stress–strain curve under uniaxial pulling is shown in Supplementary Fig. 9b. Despite this similarity in the equilibrated configuration, the mechanical response of the two systems differs. Unlike system $(1.9, 2.3)$, which displays highly brittle behavior due to the nearly simultaneous detachment of connected units, this system exhibits a quasi-ordered magnet detachment sequence during deformation. In the initial stages of loading, multiple

Bar units first unravel and act as inter-layer connections, as illustrated by configuration (ii) in Supplementary Fig. 9b. Upon continued loading, deformation becomes dominated by the progressive and increasingly disordered disassembly of connected Bar units and Y units, and the lattice ultimately fails in a ductile manner. The full deformation trajectory is provided in Supplementary Video 5.

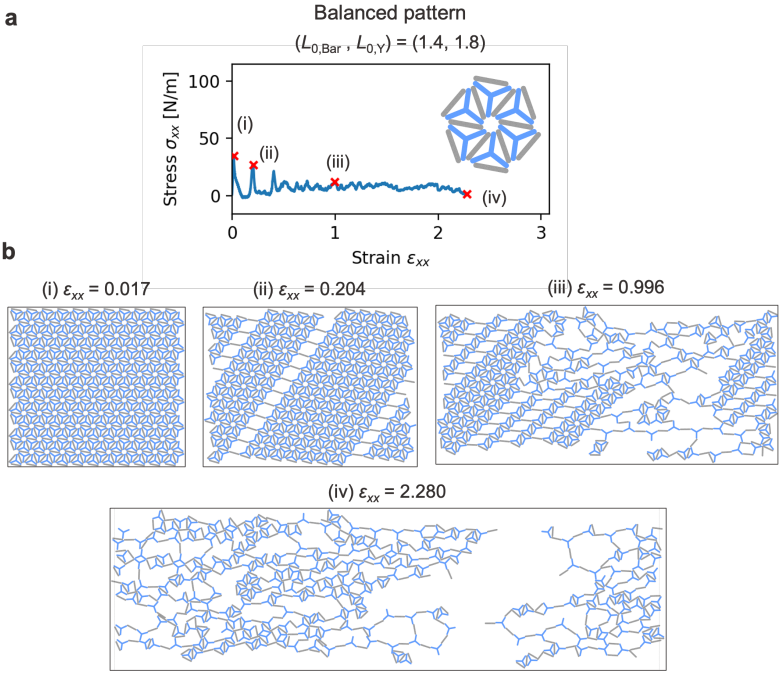

Supplementary Fig. 9 Uniaxial tensile simulation of the binary system with $(L_{0,\mathrm{Bar}}, L_{0,\mathrm{Y}}) = (1.4, 1.8)$. a, Stress–strain curve under loading. The inset shows its magnetic cluster configuration, consisting of six Y units and twelve Bar units. b, Representative deformed configurations at the strains marked by red crosses in panel a.

Notably, this system is located at the boundary of region II, adjacent to the expanded regime (region E, gray) of the phase map. This boundary position gives rise to transitional mechanical behavior that differs from that of system $(1.9, 2.3)$ in the main text, which lies near the center of region II and exhibits highly brittle failure despite forming a similar magnetic cluster after equilibration. The enhanced tensile extensibility observed here reflects a transition from the behavior of contracted balanced networks toward that of expanded lattices.

5 Data-driven prediction workflow

5.1 Geometric descriptors for cluster configurations

The magnetic cluster configuration of each binary system is described by six geometric parameters: the center coordinates of a reference Bar unit (X_{Bar}, Y_{Bar}) and the Y unit above it (X_{Y}, Y_{Y}), together with their orientation angles (θ_{Bar}, θ_{Y}) (Fig. 5a of the main text). Because most clusters exhibit rotational symmetry, we fix the reference by setting $Y_{\mathrm{Bar}} = 0$ to remove one redundant degree of freedom. The remaining five parameters form a minimal representation that uniquely defines the magnetic cluster and enables reconstruction of the full reciprocal binary superlattice via periodic replication of the unit cell.

When the size contrast between the two units becomes sufficiently large, rotational symmetry may break down because the smaller unit gains increased positional freedom in the primary lattice and can adopt multiple stable configurations. In such cases, the predicted cluster configuration corresponds to only one of several feasible states.

5.2 Multi-output GP for cluster configuration prediction

The accuracy of the multi-output GP models for the Bar-dominant, balanced, and Y-dominant types is summarized in Supplementary Table 2, evaluated using the mean absolute percentage error (MAPE) and mean squared error (MSE). Among the three types, the balanced case exhibits the best prediction accuracy. Most predicted geometric parameters achieve MAPE values below 0.1, indicating good agreement with ground-truth values. These results suggest that the proposed model can predict cluster configurations that are either at equilibrium or sufficiently close to equilibrium, making them suitable as simulation inputs and significantly shortening the self-assembly time.

Supplementary Table 2 Prediction accuracy of the multi-output GP models for the three cluster types with contracted configurations.

Type	**Metric**	X_{Bar}	X_Y	Y_Y	θ_{Bar}	θ_Y
Bar-dominant	MSE	2.37×10^{-3}	2.98×10^{-2}	5.51×10^{-2}	1.75×10^{-4}	5.30×10^{-3}
	MAPE	1.37×10^{-2}	5.87×10^{-2}	6.43×10^{-2}	5.69×10^{-2}	3.10×10^{-2}
Balanced	MSE	2.21×10^{-3}	2.20×10^{-3}	7.24×10^{-4}	1.67×10^{-3}	9.33×10^{-4}
	MAPE	8.64×10^{-3}	8.63×10^{-3}	8.42×10^{-3}	9.16×10^{-3}	1.52×10^{-2}
Y-dominant	MSE	5.83×10^{-3}	5.92×10^{-4}	1.26×10^{-3}	3.28×10^{-3}	1.51×10^{-3}
	MAPE	2.88×10^{-2}	8.81×10^{-3}	2.39×10^{-2}	1.59×10^{-1}	1.97×10^{-2}

5.3 Neural networks (NN) for tensile response prediction

To identify an appropriate neural network architecture and hyperparameter configuration, we conducted a grid search over different network structures and activation functions, as summarized in Supplementary Table 3. Both the input features and output targets were normalized using their respective means and variances prior to

training. The grid search focuses on the choice of activation function (Tanh, ReLU, and Sigmoid), the number of hidden layers, and the number of neurons in each layer. The learning rate is fixed at 5×10^{-4}. Model selection is based on the averaged normalized MSE of strength and toughness evaluated on the validation set. Based on this criterion, the optimal model employs the Sigmoid activation function with three hidden layers containing 16, 32, and 16 neurons, respectively, as highlighted in Supplementary Table 3. This model achieves test-set performance of $R^2 = 0.97$ for strength and $R^2 = 0.70$ for toughness, with an averaged MSE of 0.159.

Supplementary Table 3 Grid search results of neural network hyperparameter settings evaluated on the validation set.

Hidden sizes	**Activation**	R^2		MSE		**Avg. MSE**
		Strength	Toughness	Strength	Toughness	
[16]	ReLU	0.620	0.280	0.359	0.711	0.535
[16]	Tanh	0.843	0.526	0.148	0.468	0.308
[16]	Sigmoid	0.677	0.349	0.305	0.642	0.474
[32]	ReLU	0.789	0.363	0.200	0.628	0.414
[32]	Tanh	0.827	0.087	0.163	0.901	0.532
[32]	Sigmoid	0.774	0.426	0.214	0.566	0.390
[16,16]	ReLU	0.812	0.579	0.178	0.416	0.297
[16,16]	Tanh	0.944	0.495	0.053	0.498	0.276
[16,16]	Sigmoid	0.930	0.754	0.066	0.243	0.155
[32,16]	ReLU	0.833	0.445	0.158	0.547	0.353
[32,16]	Tanh	0.845	0.327	0.146	0.664	0.405
[32,16]	Sigmoid	0.857	0.642	0.135	0.353	0.244
[32,32]	ReLU	0.893	0.605	0.100	0.390	0.245
[32,32]	Tanh	0.834	0.462	0.157	0.531	0.344
[32,32]	Sigmoid	0.915	0.731	0.080	0.265	0.173
[16,16,16]	ReLU	0.805	0.647	0.184	0.348	0.266
[16,16,16]	Tanh	0.821	0.595	0.169	0.400	0.285
[16,16,16]	Sigmoid	0.847	0.658	0.144	0.337	0.241
[16,32,16]	ReLU	0.789	0.504	0.199	0.490	0.344
[16,32,16]	Tanh	0.835	0.551	0.156	0.443	0.299
[16,32,16]	**Sigmoid**	**0.962**	**0.904**	**0.036**	**0.095**	**0.066**

5.4 NN-predicted strength and toughness

The NN-predicted strength and toughness across the entire design space are shown in Supplementary Fig. 10. Discontinuous regions correspond to geometries classified as expanded by the trained GPC and are therefore excluded from NN prediction. The predicted property landscape is consistent with trends observed in the dataset (Fig. 4a,b of the main text).

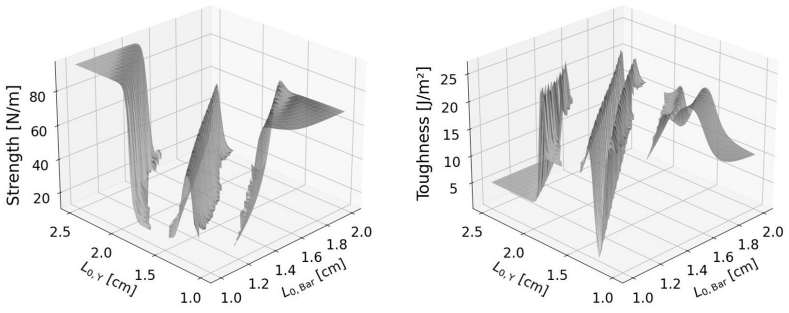

Supplementary Fig. 10 Strength (left) and toughness (right) predicted by the neural network over the entire design space.